

UV/VUV emission from a high power magnetron sputtering plasma with aluminum target

E. J. Iglesias^{1,3}, A. Hecimovic^{2,4}, F. Mitschker¹, M. Fiebrandt¹, N. Bibinov¹ and P. Awakowicz¹

¹ Institute for Electrical Engineering and Plasma Technology, Ruhr-University Bochum, Universitätsstraße 150, 44801, Bochum, Germany.

² Institute for Experimental Physics II, Ruhr-University Bochum, Germany

³ Departamento de Física, Universidad Simón Bolívar, Caracas, 1089, Venezuela

⁴ Current address: Max-Planck Institute for Plasma Physics, Garching, Germany.

E-mail : Enrique.Iglesias@ruhr-uni-bochum.de and ante.hecimovic@ipp.mpg.de

Abstract

We report the *in situ* measurement of the ultraviolet/vacuum-ultraviolet (UV/VUV) emission from a plasma produced by high power impulse magnetron sputtering with aluminum target, using argon as background gas. The UV/VUV detection system is based upon the quantification of the re-emitted fluorescence from a sodium salicylate layer placed in a housing inside the vacuum chamber at 11 cm from the center of the cathode. The detector is equipped with filters that allow for differentiating various spectral regions, and with a front collimating tube that provides a spatial resolution ≈ 0.5 cm. Using various views of the plasma, the measured absolutely calibrated photon rates enable to calculate emissivities and irradiances based on a model of the ionization region. We present results that demonstrate that Al^+ ions are responsible for most of the VUV irradiance. We also discuss the photoelectric emission due to irradiances on the target $\sim 2 \times 10^{18} \text{s}^{-1} \cdot \text{cm}^{-2}$ produced by high energy photons from resonance lines of Ar^+ .

Keywords: magnetron sputtering, HiPIMS/HPPMS, ultraviolet/vacuum-ultraviolet, sodium salicylate, absolute calibration, in situ, photoemission.

Introduction

Investigations in various low-pressure and low-temperature industrial plasmas [1] have revealed synergistic effects on film characteristics produced by these plasmas [2]. These effects are caused by particle bombardment and heating of the substrate, as well as by UV/VUV photons in the energy range from 3 eV to 12 eV. For example, Shin et al. [3] have demonstrated that in a chlorine containing etching plasma, there is a substantial etching below the ion-assisted etching threshold due to VUV photo-assistance. Synergistic effects are also present on the deposition process and surface performance of deposited films of poor thermolabile materials, e.g., as polymers [4]. For this reason, there is also a comparable effort on modeling of low-pressure inductively coupled plasmas (ICP) [5,6] to systematically estimate relative fluxes of ions and VUV photons and the related control parameters.

High power impulse magnetron sputtering (HiPIMS) is a well-established technology for deposition of thin films with good adhesiveness and high density [7]; it is also especially successful on substrates with complex geometry. The electron density in HiPIMS plasmas is several orders of magnitude higher compared to DC magnetron sputtering, thus the ionization rate of the total particle flux is up to 85% [8]. The properties of the deposited film, particularly the microstructure and crystallinity, benefit also from a better control of the energy of ions impinging on the growing film [9]. However, ionic and neutral fluxes not only determine the properties of the deposited film (substrate). The infrared (IR) radiation emitted by the target (cathode) is also contributing to the total energy delivered to the deposited film during the growth, as shown by Cormier et al. [10]. The contribution of IR is largest -up to $600 \text{ mW} \cdot \text{cm}^{-2}$ - when the magnetic field configuration of the magnetron is balanced.

The HiPIMS plasma is not homogeneous but it forms self-organization patterns of localized spokes (also called *ionization zones*), rotating at frequency of $\sim 100 \text{ kHz}$ [11]. During our experiment, acquisition times are longer than 5 ms; therefore, the rotation of the spokes is smeared out producing an emission pattern in the shape of a timewise quasi homogeneous half torus that follows the so called target *racetrack*. The racetrack is the

region on the target where the HiPIMS current is maintained by single charged ions and secondary electrons released in the sputtering process [12]. Under the present experimental conditions the racetrack has a radius of about 13.5 mm, and it is about 1 cm wide [13].

From the near infrared (NIR) to the VUV, most of the emission in a HiPIMS plasma is concentrated in this half torus shape over the target. Due to the high amount of sputtered particles present an *in situ* measurement of the UV/VUV on the target is difficult. However this measurement is possible by placing a layer of sodium salicylate (NaSal) [14] near the aluminum target, and then, measuring the re-emitted fluorescence signal produced by photons reaching this layer. The *UV/VUV detector* is a housing that contains the NaSal layer and has a collimating tube that also provides protection from the contamination of sputter particles. Cut-off filters placed in front of the NaSal layer supply a broadband spectral capability to the detector.

This investigation aims at finding the origin of the observed UV/VUV radiation and its dependence on the discharge current. The UV/VUV detector cannot resolve the presence of particle radial gradients with a scale below 0.5 cm; therefore photon rates are measured using various views and positions, in order to determine the emission boundaries. Accordingly it is proposed that all the radiation is originated from a quasi homogeneous *cylindrical plasma* localized next to the target surface, which is characteristic of the so called *ionization region*. This region is confined to the magnetized region of the discharge, which extends about 1.4 cm away from the target in this experiment[13].

From this model, effective emissivity values at various spectral ranges are inferred and then, used in a calculation of irradiance along the magnetron axis and at the target surface. Due to the high VUV irradiance found at the target, the possibility of secondary electrons produced by photoemission is addressed. This photoemission is present not only inside the racetrack but also outside, where the plasma is not confined by the magnetic field.

Section 2 describes the experimental set up and the measurement procedure; the technique is discussed in more detail in reference [14]. Section 3 presents the measurements and a qualitative discussion of the UV/VUV radiation production trends

versus variation of pulse peak current and line of sight. Section 4 reports the calculations of emissivities and irradiances that lead to an estimate of the photoelectric emission from the target. The impact of these results is discussed in terms of the limitations of the analysis and measurements. A comparison to previous comprehensive observations of VUV emission produced by low-pressure low-temperature plasmas is also discussed in section 4. Finally, we conclude in section 5.

2. Method and Experimental setup

2.1. The method

The NaSal layer is a scintillator with constant quantum efficiency [15] in the spectral range between 50 nm to 325 nm (namely photon energy between 24 eV and 3.8 eV). The produced fluorescence is a broadband spectral distribution that extends between 350 nm and 550 nm, and has a maximum at ≈ 425 nm. Above 350 nm NaSal has a constant reflectance versus wavelength up to the NIR spectral range [16]. This property provides the detector with the possibility of measuring spectrally resolved line emission above 350 nm.

The fluorescence intensity is proportional to the number of photons irradiating the NaSal layer in the spectral range $\lambda < 325$ nm. Using cut-off filters in the line of sight, it is possible to differentiate the *spectrally associated fluorescence* of different UV/VUV spectral regions, as well as quantify the corresponding photon rate, $\Phi[\text{s}^{-1}]$. To contribute to a better understanding of the measurement process, figure 1 shows the spectra collected from a NaSal layer exposed to the plasma under different filter conditions. Spectrum 1(A) is the result of using a background filter, with cut-off $\lambda < 325$ nm; details are shown on table 1. Spectrum 1(B) is recorded with no filter, and 1(C) shows the selected fluorescence spectrum when 1(A) is subtracted from 1(B). As it unfolds on spectrum 1(A), the background filter prevents the production of fluorescence photons and allows for differentiating of the fluorescence spectrum from reflected emission lines that fall in the same range. The spectrum in 1(A), taken with the background filter, is named *background spectrum*.

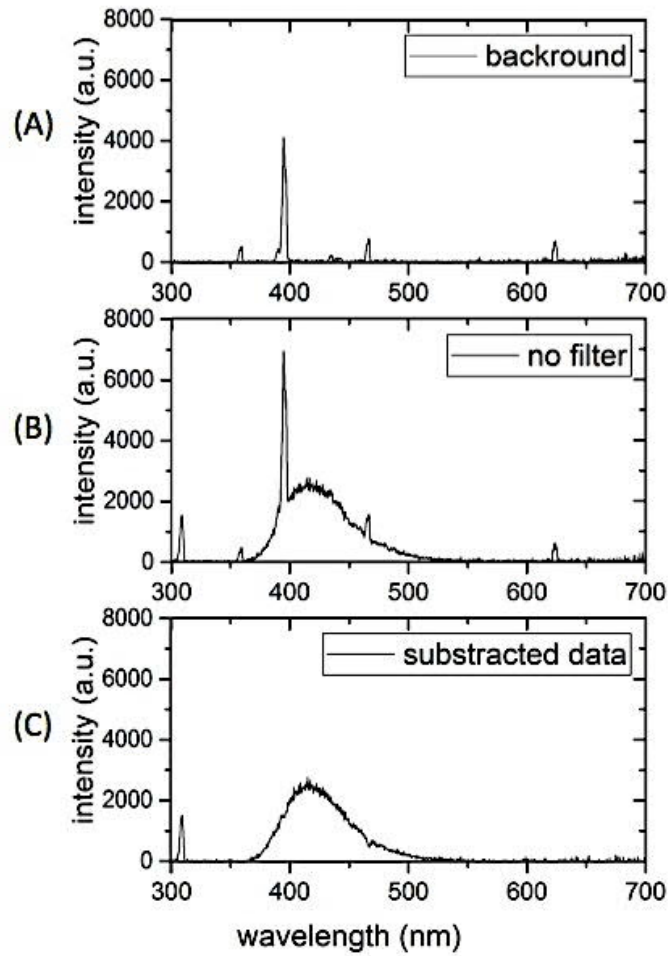


Figure 1: Illustration of the method. Sample spectrum taken parallel to the target surface for a 54 A discharge current using a low resolution spectrometer. (A) Spectrum taken with the background filter, cut-off $\lambda > 325$ nm and (B) with no filter in place. (C) Is the numerical subtraction of spectrum (B) - spectrum (A), and shows the fluorescence signal produced by photons with $\lambda < 325$ nm that impinge upon the NaSal layer.

Table 1: Description of filters.

Filter name	Transmission	Specifications
-------------	--------------	----------------

BaF ₂	>135 nm	Korth Kristalle Gmbh
Quartz	>225 nm	Herareous Quartz Glass Gmbh, M235
Background	>325 nm	Asahi Long Pass Filter, ZUL0325

2.2. Experimental setup

The experimental setup consists of a 5 cm diameter (20 cm² area) circular planar magnetron mounted in a cylindrical chamber, 40 cm in diameter, and 40 cm in height. The target material is aluminum, and the pressure of argon gas in the chamber is kept at 0.5 Pa. The voltage is ON during 200 μs, at a repetition frequency of 10 Hz. The discharge power variation consists of adjusting the discharge voltage to obtain peak discharge currents in the range from 5 A to 54 A; the corresponding discharge current densities (calculated over whole target surface) vary from 0.25 A · cm⁻² to 2.7 A · cm⁻². Figure 2 shows a typical discharge voltage pulse of ~200 μs in duration for the 54 A peak current case, and several current waveforms. The current onset is known to be affected by the voltage and target material [17]; the current time duration in these experiments is ~200 μs for peak current > 20 A, ~160 μs for 10 A, and ~130 μs for 5 A.

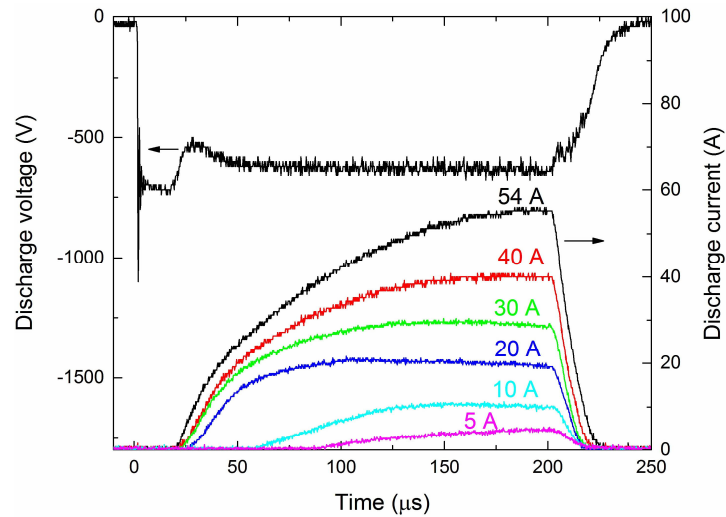


Figure 2: Current and voltage (for 54 A case) waveforms of the discharge pulse.

The detector, depicted in figure 3, houses a steel disk with a layer of NaSal that is produced by the precipitation of NaSal crystals from a 0.1 molar solution of sodium

salicylate in ethanol. The normal to the surface is oriented at 45° of the line of sight. In the front, there is a collimating cylinder of 72 mm long with 6 mm inner diameter that produces a 5° degree acceptance cone. The cylinder and a front mesh with $\sim 50\%$ transmittance, protect the NaSal layer from getting coated and determines the spatial resolution. The front end of the collimating cylinder is placed at the edge of the cylindrical aluminum cathode.

The light produced at the NaSal layer is collected and guided by an optical fiber and vacuum feedthrough to one of two spectrometers placed outside the vacuum chamber. One setup is an USB *grating spectrometer* (Avantes AvaSpec-ULS2048XL) with a wavelength range from 200 to 1100 nm, and a *low spectral resolution* $\Delta\lambda = 3$ nm. With this spectrometer, the fluorescence spectrum (broadband) and spectral lines are captured within the same intensity scale (figure 1); however, weak atomic lines are merged into the background. The second spectrometer is the absolutely calibrated *echelle spectrometer* (ESA 3000, LLA Instruments, Germany) with an spectral expand from 200 nm – 800 nm [18] and a *high spectral resolution* of $\Delta\lambda \approx 30$ pm at 450 nm. Due to the high resolution of the echelle spectrometer, the amount of counts per pixel for the broadband emission is low. Therefore, it is necessary to collect a number of discharge pulses to achieve a good signal to noise ratio of the fluorescence spectrum. Weak and narrow lines of all species in the plasma can be detected with this spectrometer due to its high dynamic range.

None of the spectrometers provide time resolution within the time frame of one current pulse. The grating spectrometer is gated ON during 1 second, resulting in the average of 10 discharges; this procedure is typically repeated 10 times. The echelle spectrometer is synchronized with the high voltage pulse, and it is gated ON during 5 ms in every discharge. Discharges are accumulated up to 200 times for a good signal to noise ratio on the broadband fluorescence spectrum. The inferred photon rates using the echelle spectrometer are calculated using the corresponding pulse duration time in each case.

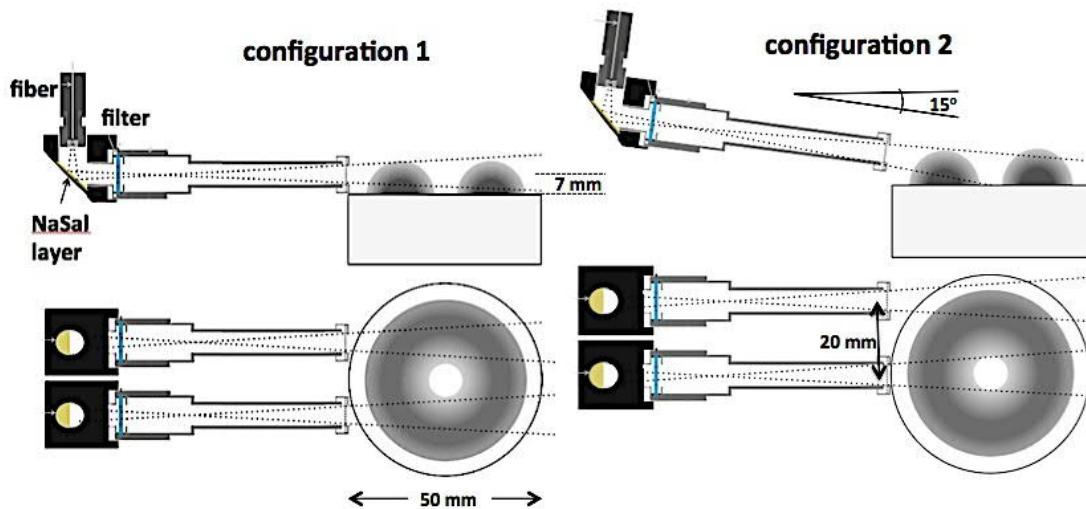


Figure 3: Optical emission spectroscopy setup, configuration 1 (Conf.1) and configuration 2 (Conf.2). In configuration 1, both detectors are placed parallel and symmetrically at 1 cm on both sides of the magnetron axis, and at 7 mm above the target surface. In configuration 2, both detectors are aimed at the cathode at 15°, one detector at the center, the other close to the edge at 2 cm from the axis. The two detectors are 2 cm apart. The circular gray zone is an idealization of the toroidal ionization region.

Two detectors are used to enhance the efficiency of the measurement process, shown in figure 3. The equivalence of both detectors is tested comparing the fluorescence measured with no filter in a 54 A current plasma in Conf.1. The intensities in both spectra are found to be within 10%. The detectors are positioned in two line of sight configurations. For *configuration 1* (Conf.1), both detectors are parallel at 7 mm above the target surface, and are located 2 cm apart on both sides of the magnetron axis. Conf.1 is applied to the measurement of line intensity and fluorescence trends when equipped with the low resolution spectrometer; it is also utilized for calibration, with 54 A peak current plasma, with the absolute calibrated echelle spectrometer. The detectors in *configuration 2* (Conf.2) are oriented at 15° with respect to the surface of the target and are aimed at the racetrack. In Conf.2, detector 1 looks along the center line of the magnetron, while detector 2 covers the edge and the outer part of the magnetron at 2 cm from the center. In the following, we will append to the abbreviations Conf.1 and Conf.2, the terminology cent/edg/off and ech/gra to refer to center, edge or off axis detector and to echelle or grating spectrometer.

2.3. Filters and differentiated spectral ranges

BaF₂, quartz, background and no-filter, are the filter used along the detector line of sight; see table 1 for details. The subtraction spectra taken with two different filters allows the following spectral ranges (SR) to be differentiated: (SR1) $\lambda < 135$ nm, (SR2) $135 < \lambda < 225$ nm, (SR3) $225 < \lambda < 325$ nm, (SR4) $\lambda > 325$ nm. The subtraction is performed taking into account the filter factors presented in table 2. These filter factors are the result from averaging the transmittance in every spectral range, using the curves presented in figure 4.

Table 2: Filter transmission factors used in spectral subtraction for the different spectral bands. The values for BaF₂ and for Quartz $\lambda < 325$ nm are average values inferred from figure 4

Transmission [%]	*SR1 $\lambda < 135$ nm	SR2 $135 < \lambda < 225$ nm	SR3 $225 < \lambda < 325$ nm	SR4 $\lambda > 325$ nm
No-filter	100	100	100	100
BaF ₂	0	88 ± 4	93 ± 2	93 ± 2
Quartz	0	0	78 ± 4	91 ± 2
Background	0	0	0	91 ± 2

*Spectral Range

The BaF₂ filter -with a cut-off $\lambda \sim 135$ nm- defines the upper end of SR1, and also coincides approximately with the low wavelength end of the Al⁺ ion observable spectrum, as presented in spectral data tables [19]. Thus, the use of the BaF₂ filter differentiates the emitted photons from Al⁺ from those originated from Ar and Ar⁺ below 110 nm. Most of the tabulated spectrum Al⁺ falls in SR2, and also the most intense lines of Al⁺⁺. SR3 is the UV spectral range and is dominated by the Al resonance lines, and with a lesser contribution from Al⁺ lines. SR4 is differentiated using the background filter –cut-off $\lambda > 325$ nm. In SR4, the fluorescence signal is found, as well as spectral lines from radiation reflected off the NaSal layer. The Al 394.4 nm resonance line is the strongest observable line in SR4, together with various NIR argon lines above 690 nm. When the background filter is used, there is no fluorescence, while the resulting background spectrum is utilized for subtraction from spectrums taken with other filters in order to separate the broadband fluorescence. Various technical details relevant to this technique are illustrated in figure 4. The spectrums on figure 4, for $\lambda < 225$ nm, are synthetic and shown only for guidance. Descriptions of the indicated spectral lines are presented in table 3.

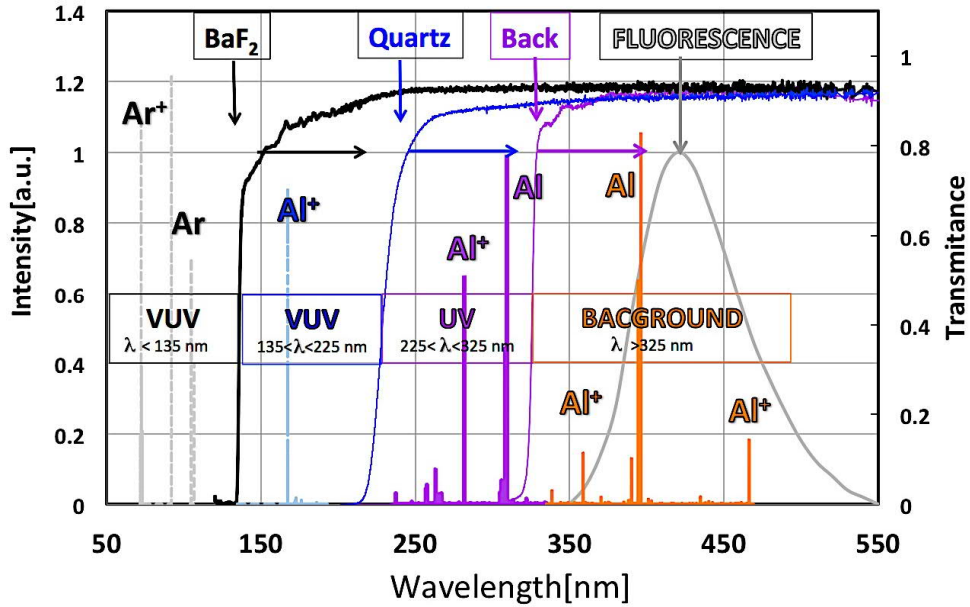


Figure 4: Filters transmission curves and expected spectrum from a HiPIMS aluminum/argon plasma. The spectrum $\lambda > 225$ nm (in arbitrary units left axis) corresponds to an observed spectrum looking into the HiPIMS Al/Ar plasma, parallel to the target with no NaSal layer in place. Below $\lambda < 225$ nm, the light-dashed lines are a synthetic spectra - from NIST database [19]- and are used only for guidance (relative intensities do not respond to any particular model calculation). The broadband feature that peak at 420 nm (light gray) is a depiction of the fluorescence spectrum produced by the NaSal. Also shown are transmission curves (right axis) of BaF₂ (black), quartz (blue) and background (magenta) filters. Information of about the spectral lines is presented on table 3.

Table 3: Most intense emission transitions of Al, Al⁺, Al⁺⁺, Ar, Ar⁺ in expected in an Ar/Al HiPIMS spectrum.

Discriminating filter	Spectral range [nm]	Spectral features (term- λ □ nm □)
No filter- BaF ₂	$\lambda < 135$	Ar ⁰ (3p ⁵ 4s-3p ⁶) – 104.8, 106.6 Ar ⁺ (3s3p ⁶ -3s ² 3p ⁵) – 92.0
BaF ₂ - Quartz	135 < λ < 225	Al ⁺ (2p ⁶ 3s3p -2p ⁶ 3s ²) – 167.1 Al ⁺⁺ (2p ⁶ 3p -2p ⁶ 3s) – 185.5
Quartz - Background	225 < λ < 325	Al ⁰ (3s ² 3d -3s ² 3p) – 308.2, 309.3 Al ⁺ (3s4s -3s3p) – 281.6
Background	$\lambda > 325$	Al ⁰ (3s ² 4s -3s ² 3p) – 394.4, 396.2 Al ⁺ (3s4f -3s3d) – 358.6 Ar ⁰ (3p ⁵ 4p->3p ⁵ 4s) > 690.0

2.4. Absolute calibration

The goal of the absolute calibration is to find the magnitude of the incoming flux of photons, that corresponds to a measured fluorescence in [#counts · s⁻¹]. This calibration is made *in situ* by following two steps. First, the fluorescence count rate Φ_A in [#counts · s⁻¹] is measured with the setup shown in figure 5(A), with the NaSal layer in place. Next, the magnitude of the corresponding incoming photon rate Φ_B in [#phots · s⁻¹] is measured, with the setup shown in figure 5(B). Both measurements are made in the region from 225 to 325 nm (SR3), in Conf.1-off-ech. The final calibrated photon rate in A is Φ_A^{cal} and is given by the following formulas:

$$\Phi_A^{cal} = \Phi_A \cdot K_{cal} \quad (1)$$

$$K_{cal} = \frac{\Phi_B \cdot g}{\Phi_A}$$

where g is a geometric factor that takes into account the differences in the light collecting characteristic among set up A and B. K_{cal} [#photons/#counts] is the calibration constant that transduces the fluorescence count rate into its corresponding photon rate. Due to the constant quantum efficiency of NaSal for 50 nm < λ < 325nm [15], the same calibration constant K_{cal} is used for the two VUV spectral ranges SR1 and SR2.

In practice two spectra are first measured using the set up in figure 5(A), one with the quartz and another with the background filter. The spectrally associated fluorescence rate Φ_A corresponding to SR3, is calculated by subtracting the spectrum obtained with the background filter from the spectrum obtained with the quartz one; the resulting spectrum is integrated between 350 nm and 550 nm. Then, the NaSal layer is set aside from the detector, and an absolute incoming photon rate Φ_B in SR3 is measured directly with the calibrated echelle spectrometer with the set up 5(B).

The geometrical factor $g = f_1 \cdot f_2$, where f_1 is the ratio of the two collecting areas of the detectors, (diameters shown on figure 5) and f_2 is the ratio of the acceptance cone volumes of both systems, thus $g = 35$. The maximum error on the estimation of the geometric factors (described above) is 25%. The errors in the analytical process of the experimental spectrum that are caused by the background value, signal to noise ratio, and

the filter values add another 25%. Finally, the error of the intensity measurements using the calibrated echelle spectrometer amounts to 16% [18]. The total error on the measurement of Φ amounts to 45%.

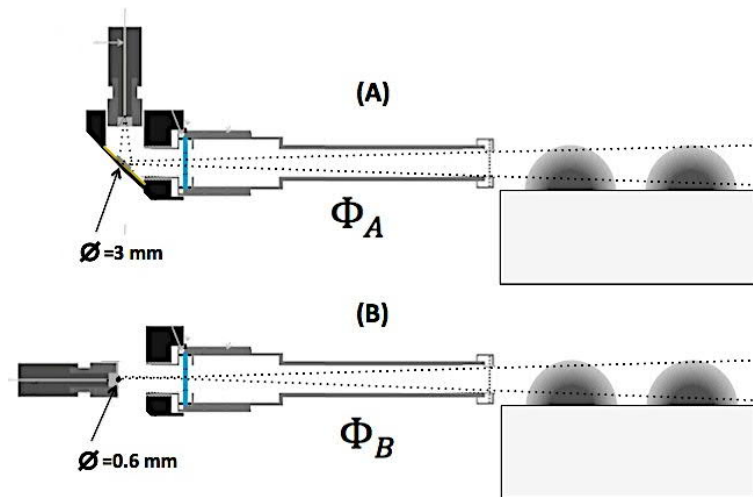


Figure 5. Absolute calibration in Conf.1-off-ech (A) Detector parallel to the target with the NaSal layer in place, to measure Φ_A . (B) Detector parallel to the target, looking directly into the plasma with no NaSal layer, to measure Φ_B . The absolute calibrated echelle spectrometer [18] is used in both conditions. The figure also indicates the diameter of the sensing areas used for the calibration procedure.

3. Trends of line emission and photon rates versus pulse peak current

3.1. Visible/UV emission trends versus pulse peak current

Figures 6(A) and 6(B) show the relative trends of time and wavelength integrated intensities of spectral lines versus peak current. These trends are the result of averaging the intensity of groups of lines from the various emitting species in the plasma (see table 4). Due to the considerable differences in intensity among the lines from the various species, these lines were measured with the echelle spectrometer in Conf.2-cent-ech. The relative intensities are normalized to a value at 54 A and also to the variation on the exposure time due to the current pulse length. The main criteria for choosing the lines are the signal to noise ratio and to avoid the effect of saturation.

Table 4: Wavelength[nm] of emitted lines used in figures 6(A),6(B).

Specie	Term	Wavelength [nm]
Ar	$3s^23p^5$ (4p - 4s)	750.3, 772.4, 801.5
Ar ⁺	$3s^23p^4$ (4p - 4s)	434.8
Al	$2p^63s^2$ (5d - 3p) (5s - 3p)	226.34, 226.90 266.0
Al ⁺	$2p^63s$ (4f - 3d) (4d - 4p) (4p - 4s)	747.3 559.3 705.7, 706.4
	$2p^6$ (3p ² -3s3p)	390.1
Al ⁺⁺	$2p^6$ (4d - 4p) (4p - 3d)	451.3, 452.9 361.2

Figure 6(A) shows that for plasmas produced with peak pulse currents below 10 A, the Ar emission increases with current. Above 10 A, a tapering of the lines intensity is observed. The reduction of Ar intensity above 10 A is a consequence of two effects: rarefaction of Ar in the target vicinity due to sputtering wind [20, 21] and increase of the plasma density that is further depleting Ar metastables by ionization [22,23]. Ar⁺ emission shows a monotonic increase. Above After 20A, both Ar and Ar⁺ emission exhibit saturating trends, and as shown in figure 6(B), the power delivered to the discharge is deposited in increase of the first and second ionization state of Al. Even though higher currents results in higher density of the sputter wind, one could expect consequent reduction of all Ar intensity due to stronger Ar rarefaction. Anders et al. [Anders et al. J. Phys. D: Appl. Phys. 45 (2012) 012003] suggested that significant number of Ar gets re-sputtered from the target in a so called “recycling trap” which results in continuous presence of Ar in the target vicinity and saturated emission signal.

Figure 6(B) shows an increase of the Al⁺ and Al⁺⁺ emission (ionization energy 6 eV and 18.8 eV, respectively) above 10 A suggesting a strong ionization of the Al atoms sputtered from the target. Like Ar⁺ ions, Al⁺ and Al⁺⁺ should be close to the target surface, in the ionization region [24]. The emission for Al starts to saturate at 20 A due to the strong electron collisional ionization and Penning ionization by metastable argon atoms (energy 11.9 eV) [20], that lead to the high ionization degree in HiPIMS. It should be noted that the intensity of the Al⁺⁺ lines is very low, as well as the density due to the relatively high ionization potential of Al⁺[25].

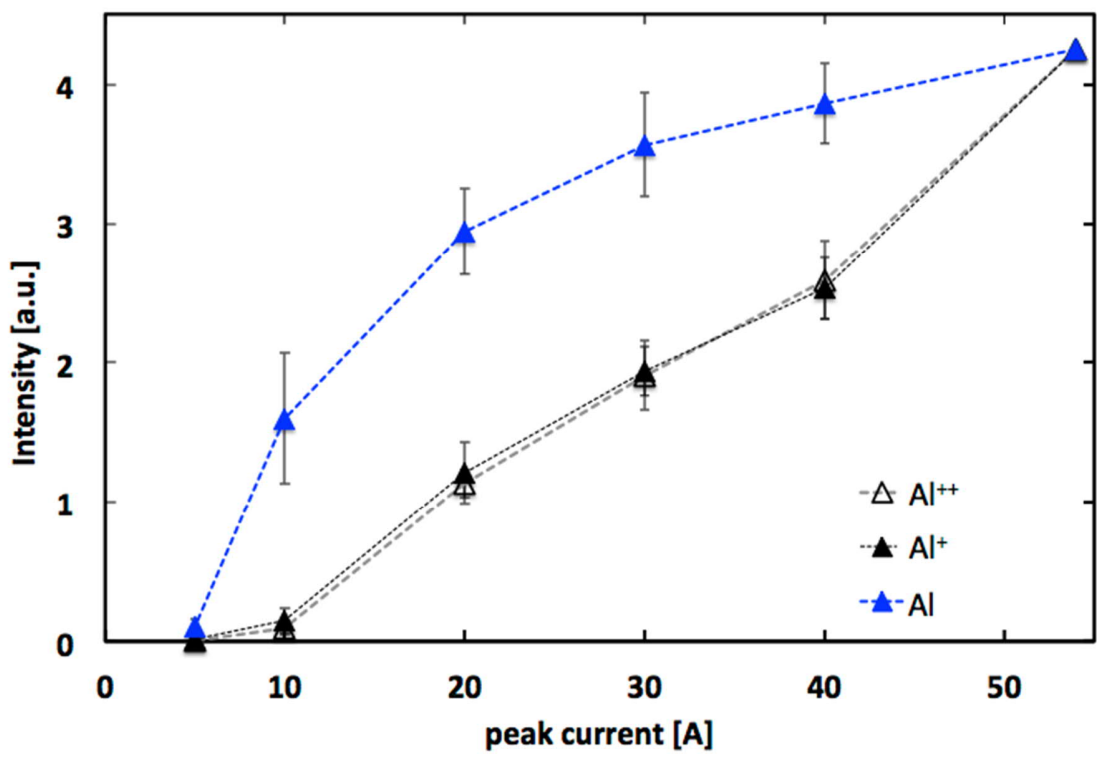
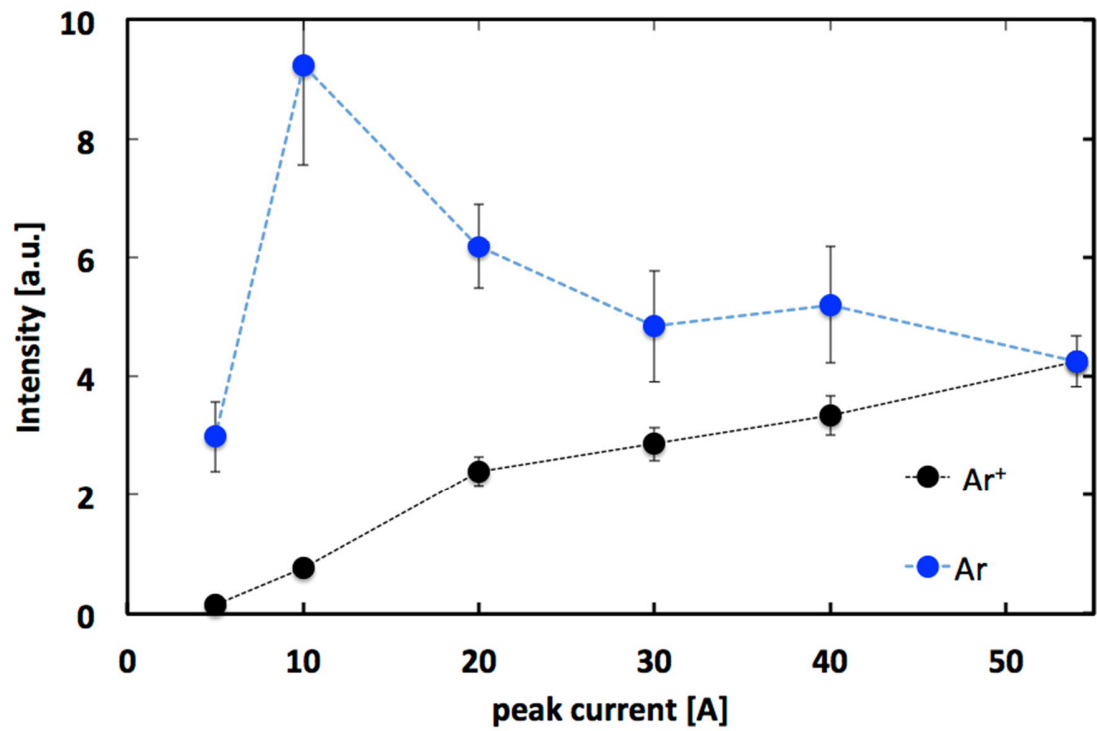


Figure 6. Relative trends of time integrated line collected using Conf.2-cent-ech. The traces respond to the average intensity of groups of lines emitted by the various species. (A) Ar (blue) and Ar⁺, and (B) Al(blue), Al⁺, and Al⁺⁺. The actual intensity values vary considerably so all the traces are normalized to the same value at peak current 54 A. Details of the emission lines used are found in table 4.

3.2 VUV absolute photon rate trends versus peak current

The measured photon rates (from the corresponding spectrally associated fluorescence) are shown in figure 7. They correspond to the emission of atoms and ions within the acceptance cone defined by the detector. Considering the available fluorescence intensity, two sets of measurements are performed: one set using the center detector from angled Conf.2-cent-ech (solid lines), and another set from parallel Conf.1-off-gra (dashed lines). For a peak current of 5 A, the recorded fluorescence is within the signal noise for both setups. To achieve a relative comparison of the parallel and angled views of the plasma -with the two different spectrometers-, the fluorescence in SR3 is measured using the echelle spectrometer in Conf.1-off-ech at 54 A. The resulting calibration point is shown in the figure 7. The logarithmic scale is used for convenience to illustrate both sets of measurements simultaneously.

The comparison in figure 7 shows lower fluorescence for the parallel view (Conf.1-off-gra) that corresponds to a lower density of the plasma species further from the target; this fact is frequently reported in the literature. The magnitude of this decrease changes with the spectral range, and is largest for the UV and VUV. However, since the Conf.2-center, and Conf1-off are offset by 1 cm, it is difficult to correlate these observations more precisely.

The edge view (not shown), Conf.2-edg-ech, was also measured. This view at 2 cm from the magnetron axis (0.5 cm from the edge of the target) intersects only partially the ionization region, and the resulting total photon rates, measured with no-filter, are about 0 - 20% of those measured at the center, depending on the spectral range. The spectrum in this spatial region shows no presence of Ar⁺ and Al⁺⁺, while Al⁺ is very much reduced. Therefore, at the target edge, all UV/VUV radiation decreases considerably, and this happens because neither hot nor a high-density electrons are present. The comparative

results, of Conf.2-edg-ech and Conf.1-off-gra, with respect to the center view Conf.2-cent-ech, demonstrates that the light emitting plasma is confined to an area close to the target, whose outer radius extends most probably to the edge of the race track about 2 cm from the magnetron axis.

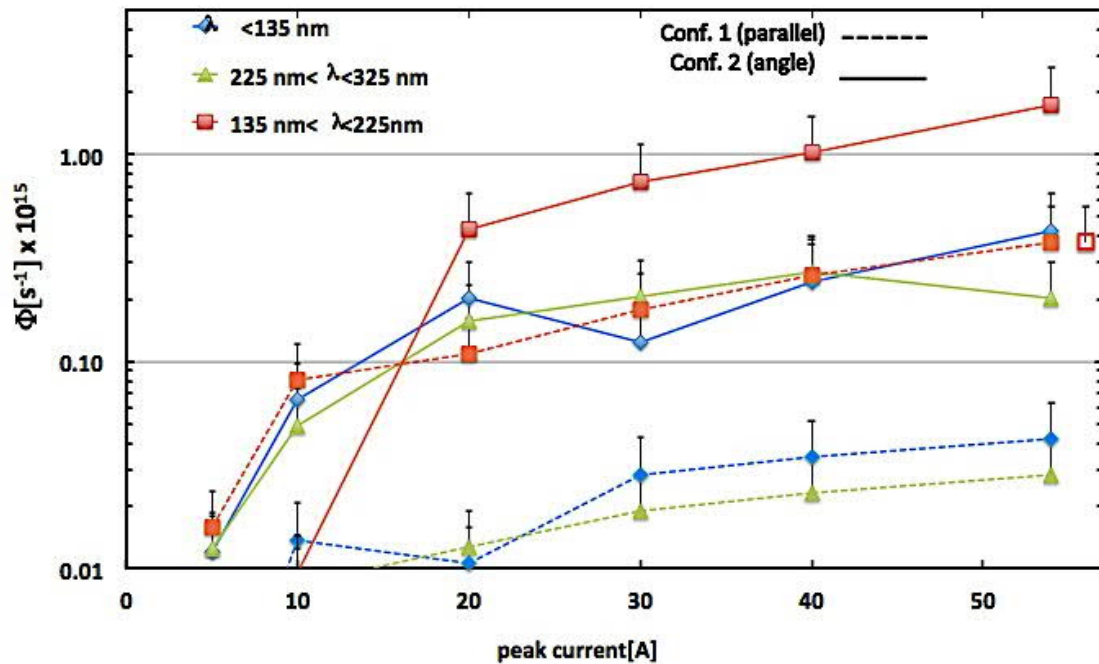


Figure 7. Trends of two views of the time averaged photon rate (Φ) produced by atoms and ions within the acceptance cone of the detector. View one is Conf.2-cent-ech (solid lines), and view two is Conf.1-off-gra (dashed lines). The (red empty square) is a calibration point using the echelle spectrometer at a peak current of 54 A, at SR3 in Conf.1-cent-ech. This point is shifted ad hoc in peak current value for the sake of clarity. The logarithmic scale is used to illustrate both sets of measurements simultaneously, and only the positive side of the error bars is presented for convenience. Some small value points are off scale, meaning that the signal is within the noise level of the measurement.

Optical depth

The measured photon rates in the UV/VUV can originate from resonant lines; this is the case for lines from Ar, Ar⁺ and Al. Resonant lines are very prone to be reabsorbed in the plasma environment, mostly when: the absorbing plasma is dense, the optical path is large, or a combination of both. In the case of Ar, this gas is present all along the observation line of sight and the ground state density is close to the background

gas density. A simple optical depth calculation under these conditions [26], reveals a mean free path in the fractions of a millimeter for the strong resonance lines of argon at 104.8 and 106.7 nm. Therefore, at the detector the corresponding photon rate will be strongly reduced because this resonance radiation is absorbed by the argon gas and reemitted in all directions along the light path. This implies that, the measured photon rate in region SR1 should originate in Ar⁺ ions that are localized close to the target surface. Ar⁺ ions also emit into resonant transitions [27] but they have typically an oscillation strength on the order of 1% of Ar. Additionally, the plasma where these ions exist is at most a few millimeters in radial extent. Outside this region of emission, Ar⁺ density decreases very fast [24]; therefore, the possibility of reabsorption in the direction of our detector is very small. As it unfolds, the radiation reaching the target on SR1 is coming from a small region close to the target surface where Ar⁺ ions are present. However, it could be the case that some excited Ar atoms also exist in the center of the target at early stages in the discharge pulse [13].

The observed emission from Al⁺ in SR2 is the strongest, and shows in all our detector views. The strong resonant line of Al⁺ at 167.1 nm, reveals a large optical depth. However, the emission in SR2 is produced by many non-resonant lines -judging from the various transitions that are observed in the visible spectral range. The presence of non-resonant lines implies that radiation from Al⁺ has a high probability to reach both target and detectors. In the case of Al atoms, most lines that fall in SR3 are resonant lines; they can be highly absorbed since the decrease in Al density away from the target is relatively slow (in comparison to Ar⁺) and Al could be also found in the center region of the discharge [13].

4. Analysis and results

4.1 Methodology

Calculation of the effective emissivity

Noninvasive optical spectroscopy techniques can lead to a direct correspondence

between emission measurements and plasma parameters, when the plasma is homogeneous –and larger than the acceptance cone- or the plasma is point like. However, this is not possible in general, and more information about the plasma is needed. In the case of the HiPIMS plasma, the experimentally measured photon rates Φ are not only time integrated, but also the result of a line of sight effective emission.

Further, Φ is a quantity that not only depends on the properties of the source (plasma) but also on the characteristics of the collecting system, namely the acceptance cone and the detector area. For this reason, it is pertinent to shift our analysis towards emissivity $\varepsilon[\text{s}^{-1} \cdot \text{cm}^{-3}]$, a quantity that only depends on the plasma properties. In a homogeneous plasma, ε is related to Φ through the following two equations:

$$\varepsilon[\text{s}^{-1} \cdot \text{cm}^{-3}] = \frac{\Phi[\text{s}^{-1}]}{V^{\text{eff}}[\text{cm}^3]} \quad (2)$$

$$V^{\text{eff}}[\text{cm}^{-3}] = \int_V F \cdot \frac{A_{\text{det}}}{4\pi d^2} \cdot dV \quad (3)$$

where V^{eff} is an effective volume of emission that result from the integral defined in equation 3. In this equation, every differential emitting volume dV is weighted by the fractional amount of the emitted isotropic radiation -second term inside the integral- collected by the detector at the respective distance d . The total volume of emission V is defined by the acceptance cone of the detection system, see figure 8. The first term $F \sim 0.8$ [14] is a predetermined number using a goniometer measurement that takes into account the effect of the vignetting caused by the cylindrical collimator.

The collection of the various measured views of Φ , indicate that the intensity of emission not only respond to changes in peak current but also in space localization. To apply equations 2 and 3 a model of the plasma is required. Here, it is proposed a quasi homogeneous cylindrical plasma of the size of the magnetized region of the plasma, that represents the ionization region, as discussed before. This cylindrical region over the surface of the target, has a height of 1.4 cm; approximately the localization of the last magnetic close line of the trap [13]. The radius is 2 cm, the outer radius of the race track

[23]. For the experimental photon rates Φ , we use the measured rates obtained with the Conf.2-center-ech view. There the volume V on equation 3 is determined by the acceptance cone of the detector, as sketched on figure 8.

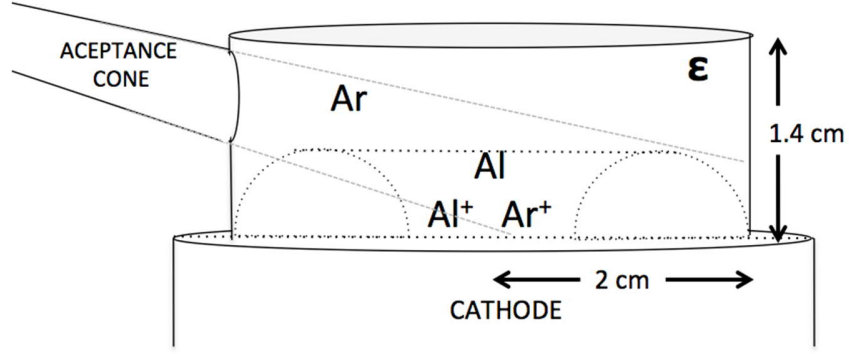


Figure 8. Sketch of the acceptance cone of the center detector and the homogeneous cylindrical plasma that represents the ionization region. The radius of the cylinder is 2 cm, and the height 1.4 cm. The torus is the timewise smeared region where spokes circulate along the racetrack.

Calculation of irradiances

Note that since the collected radiation is limited only to the plasma within the acceptance cone, the measured photon rates cannot be used to infer directly the *in situ* irradiance at the detector position. To be able to estimate total irradiances at a given point, one needs to integrate the emission from every point of the plasma using the following expression [28]

$$I[\text{s}^{-1} \cdot \text{cm}^{-2}] = \int_V \varepsilon(\vec{r}) \frac{1}{4\pi|\vec{\rho}(\vec{r})|^2} \cdot \cos(\beta) dV \quad (4).$$

Neglecting reabsorption effects, equation 4 describes the analytical procedure for calculating the irradiance $I[\text{s}^{-1} \cdot \text{cm}^{-2}]$ in a spatial point p . In the equation, V is the emitting volume and $|\vec{\rho}(\vec{r})|$ is the distance between emitter and the point p . β is an angle in three dimensions between the vector $\vec{\rho}$ and the unitary vector \hat{p} , the normal to the underlying area at point p . $\varepsilon(\vec{r})$ is the emissivity at position \vec{r} in the emitting plasma. The following figure 9 is the sketch for the calculation of the irradiance over an area placed at the target surface (grey disk), produced by the cylindrical homogenous plasma. The

outcome of this calculation is the radial distribution (vs. r) of the irradiance. The same equation can be used for the calculation at a point along the magnetron axis, at 10 cm from the target, by only changing the limits of integration.

$$I(r) = \varepsilon \times \iiint_{0,0,0}^{z_0, r_0, 2\pi} \frac{z r dz dr d\varphi}{4\pi[(x_0 \sin\varphi)^2 + (r - x_0 \cos\varphi)^2 + z^2]^{\frac{3}{2}}}$$

Figure 9. Sketch for the calculation of the irradiance on an area placed at position \mathbf{x}_0 . This sketch and equation applies also for the calculation at the point in the magnetron axis at 10 cm from the target. $r_0=2.0$ cm, and $z_0=1.4$ cm. The emissivity ε , is a constant in this calculation.

4.2 Results

Table 5 presents the results of emissivity and irradiance obtained from the model at a peak current of 54 A; further, figure 10 shows the resulting trend versus peak current. As expected both physical quantities follow the photon rate trends in figure 7 for Conf.2-cent-ech. From table 5 it is inferred that the radiation power delivered on target during one pulse (at the racetrack radius) by a 54 A peak current discharge is about $16 [W \cdot \text{cm}^{-2}] \cdot 20 \text{ cm}^2 = 320 \text{ W}$ -assuming that the irradiance inferred at the racetrack applies to the whole target surface. This value is $\sim 1\%$ of the peak power delivered by one discharge. The radiation power at a substrate at 10 cm from the target is approximately $1 \text{ W} \cdot \text{cm}^{-2}$.

Table 5. Effective emissivities and irradiances for the spectral ranges SR1, SR2, and SR3, for a 54 A peak current ($1.7 \text{ kW} \cdot \text{cm}^{-2}$), and background argon pressure of 0.5 Pa. The emissivities are inferred from the model described in figure 8. Irradiances are estimated in two positions: 1) on the aluminum cathode surface at the racetrack at radius of $r = 1.4$ cm,

and 2) at a distance of 10 cm along the magnetron axis. For the irradiances in $[W \cdot cm^{-2}]$, the following photon energies are used: ^{*}3.9 eV for SR3, ^{**}7.2 eV for SR2, and ^{***}12 eV (Ar) for SR1. The experimental error is 45%.

Peak current 54 A	SR3	SR2	SR1
Emissivity $[s^{-1} \cdot cm^{-3}] \cdot 10^{20}$	0.03	0.24	0.06
Irradiance on cathode $[s^{-1} \cdot cm^{-2}] \cdot 10^{19}$ $[W \cdot cm^{-2}]$	0.11 0.7 [*]	0.96 11 ^{**}	0.24 4.6 ^{***}
Irradiance @ 10 cm on axis $[s^{-1} \cdot cm^{-2}] \cdot 10^{19}$ $[W \cdot cm^{-2}]$	0.0064 0.039 [*]	0.054 0.63 ^{**}	0.013 0.26 ^{***}

The experimental emissivities in table 5 can be compared with simplified estimates using *only one transition*. The ground state densities of Ar^+ and Al^+ close to the target are estimated as follows $n_G^{Al^+} \sim n_G^{Al^+} \sim 0.5 \cdot n_e$, assuming that the global concentration of this ions is equal to 50% of the electron density n_e [24,29] The value of n_e corresponds to the sheath electron density $n_e \approx 6 \times 10^{13} cm^{-3}$, that was measured by Hecimovic et al. [30], -also using a 5 cm Al target, at 54 A and 0.5 Pa background argon pressure. Then $\epsilon_{Al^+} \sim 0.5 \cdot n_e^2 \cdot k_{Al^+}$, where the rate coefficient for electron impact excitation of the 167.1 nm resonant line is $k_{Al^+} = 48 \times 10^{-9} cm^3 s^{-1}$ (estimated using cross sections of Mert et al. [31] for a plasma with electron temperature of 3 eV [12]). $\epsilon_{Ar^+} \sim 0.5 \cdot n_e^2 \cdot k_{Ar^+}$, using $k_{Ar^+} = 0.2 \times 10^{-9} cm^3 s^{-1}$ for the 92 nm line, also at 3 eV [32]. The values obtained are $\epsilon_{Al^+} \sim 0.9 \times 10^{20}$ and $\epsilon_{Ar^+} \sim 0.004 \times 10^{20} s^{-1} \cdot cm^{-3}$. Both results are within the order of magnitude of the corresponding value shown for SR2 and SR1 in table 5 respectively. ϵ_{Al^+} might be over estimated due to the use of data from the strong 167.1 nm resonant line, that is probably reabsorbed in the plasma. On the other hand, the small value of ϵ_{Ar^+} in comparison to the experimental result, may be due to the use of only one line for the calculation, or the presence of Ar^+ ions early in the discharge at a higher electron temperature and density, before the Ar atoms are push away from the ionization region. A more detail discussion is beyond the scope of this work.

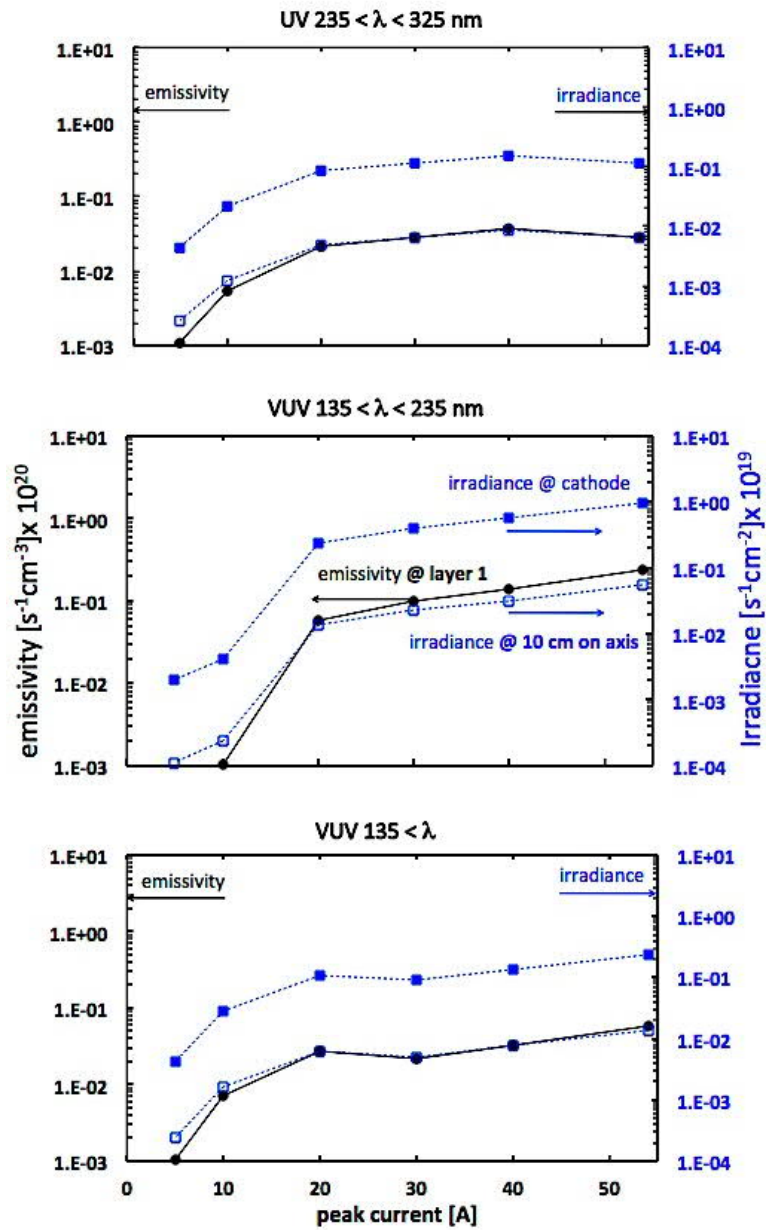


Figure 10. Trends of effective emissivities (left-black axis) and irradiances (right-blue axis) versus peak current. The solid blue square marker are the irradiance at the target race track radius and the empty square markers at a point at 10 cm from the target over the magnetron axis. Experimental errors are 45%.

Various measurements [33-37] of VUV surface irradiance produced by continuous wave ICP and pulsed MW surface wave discharges are found in the literature and can be

used for comparison. These discharges generally use argon as a working gas combined with other molecular gas mixtures, or reactive process gases. The fill pressures varied between 0.13–6.7 Pa, and the experiments have been performed at various powers. Table 6 is a summary of VUV irradiance $-\lambda < 130 \text{ nm}$ - measured in pure optically thin argon plasmas. The reported values reveal a strong correlation between both increasing electron density and increasing VUV irradiance values. In the context of this comparison, the irradiance in this work $\sim 2.4 \times 10^{18} \text{ s}^{-1} \cdot \text{cm}^{-2}$ for SR1 at the target racetrack, is comparable to the rest of the measurements in table 5. That is, when it is considered that the electron density is a factor of ~ 500 times larger [30], and the Ar^+ ions are within $< 2 \text{ cm}$ of the irradiated surface (the cathode).

Table 6: Comparative table of *in situ* absolute irradiance in units of $[10^{15} \text{ s}^{-1} \cdot \text{cm}^{-2}]$ from various experiments in argon gas.

Experiment/ year/Equipment	Type/Power [W]	n_e [10^{11} cm^{-3}]	Argon /Irradiance [$10^{15} \text{ s}^{-1} \text{cm}^{-2}$]
Woodworth /2001 VUV Spectrometer	ICP-GEC / 200	3	35 at wafer
Jinnai / 2010 Semiconductor	ICP / 1000	3	10^* at wafer
Titus / 2009 VUV Spectrometer	ICP / 200	1.3	10 at 2.5 cm above electrode surface.
Board / 2014 Vacuum diode	ICP / 600	0.5 ->10	90 at 1.3 Pa and the bottom electrode.
Peak 1998 Langmuir probe	ICP / 100	3.1	50 at plasma center.
Iglesias / 2017 NaSal detector	MW discharge 150 W 10% duty cycle	1	At wall 1.9
This work sodium salicylate detector	HiPIMS on Al 34 kW, 200 μs pulse	≤ 600	At cathode 2400 At 10 cm on axis 130

*Inferred from figure 11 [36].

4.3 Photoelectric emission from the cathode.

The secondary electron current induced by single ion bombardment of the cathode can be deduced using the following expression $J_t = J_{\text{ion}}(1 + \gamma)$, where J_t is the time averaged total current density, γ is the single ion induced secondary electron emission (ISEE) coefficient, and J_{ion} is the ion current density. The secondary electron emission is sustained

mainly by the Ar^+ ions and $\gamma \sim 0.091$ [38-39]. For a 54 A discharge, the peak discharge current density is $J_t = 6.75 \text{ A} \cdot \text{cm}^{-2}$ if J_t flows only into the racetrack [40,41] – a 1 cm wide circle that has an area of $\sim 8 \text{ cm}^2$. Therefore the corresponding current density due to the secondary electrons released in this process is $J_e = \gamma \cdot J_{\text{ion}} \approx 560 \text{ mA} \cdot \text{cm}^{-2}$.

Due to the high irradiances present at the target, there is a possibility that secondary electrons could be produced by high energy photons. The photoemission coefficient (PECoef) for aluminum in units of electron per incoming photon is strongly dependent on the photon energy, see references [42,43]. Only for energies $E_{\text{photon}} \geq 12 \text{ eV}$ ($\lesssim 100 \text{ nm}$), this coefficient has a value above 0.1. Table 7 summarizes the results from applying the corresponding factors to the radial average irradiances for each spectral range. However, it is important to note that the PECoef values do not take into consideration the intrinsic angle dependence of the photoemission process. Depending on the wavelength, the PECoef values are negligible beyond a threshold angle of incidence; this angle is measured with respect to the normal of the surface [42].

Table 7. Photo emitted currents density J_{pe} , produced by UV/VUV photons, over the target surface, for a 54 A HiPIMS plasma. PECoef is the photoemission coefficient per incoming photon [45]. J_{pe} is the photo emitted current density.

Photoemission in aluminum	SR3	SR2	SR1
Radially averaged irradiances [$\text{s}^{-1} \cdot \text{cm}^{-2}$] $\cdot 10^{19}$	0.08	0.7	0.17
PECoef [electron per photon]	$3.5 \cdot 10^{-7}$	$3.5 \cdot 10^{-4}$	0.10
J_{pe} [$\text{mA} \cdot \text{cm}^{-2}$]	$5 \cdot 10^{-5}$	0.4	28

The photoemission presents two well differentiated scenarios. One scenario is for the resonance lines of Al, Al^+ (SR2 and SR3) with a very low PECoef and a radial averaged irradiance $0.8 \times 10^{19} \text{ s}^{-1} \cdot \text{cm}^{-2}$. A second scenario where resonance lines of Ar^+ ions produce an irradiance in SR1 of $0.17 \times 10^{19} \text{ s}^{-1} \cdot \text{cm}^{-2}$, but the PECoef is comparatively ~ 300 times larger. Therefore, the photoemission current is dominated by the irradiance in SR1 producing a total of $J_{\text{pe}} = 28 \text{ mA} \cdot \text{cm}^{-2}$ for a 54 A peak current plasma, that is 5% of J_e -calculated above at peak current density. As it was discussed in section 3, SR1 radiation should be mostly produced by Ar^+ ions close to the target. For this reason, we calculated

the emissivity and irradiance for a case where the height in our model cylinder is reduced by 50%, namely 7 mm. The outcome of this calculation is that the photoemission current density is $J_{pe} = 25 \text{ mA} \cdot \text{cm}^{-2}$. The proximity of this value of J_{pe} to the previous one can be explained by the fact that the reduction in volume cancels out in the calculation. With the smaller volume, the emissivity increases but the irradiance integral is evaluated in a proportionally smaller volume too.

Since the photon irradiation can reach the entire target surface, the total photo emitted current is $\sim 0.6 \text{ A}$. In comparison, the total secondary electron current produced by ion sputtering at the racetrack -using J_e - is, $\sim 0.56 [\text{A} \cdot \text{cm}^{-2}] \cdot 8 \text{ cm}^2 \sim 4.5 \text{ A}$. In figure 10, the trend versus peak current of the secondary electron current by single ion sputtering and by photon emission from photons $\lambda < 135 \text{ nm}$ ($>9.2 \text{ eV}$) are presented. The ratio of this two currents reveals that only for peak currents $>10 \text{ A}$, i.e., in the HiPIMS regime, the photo emitted current is 10-15% of the sputtering produced one.

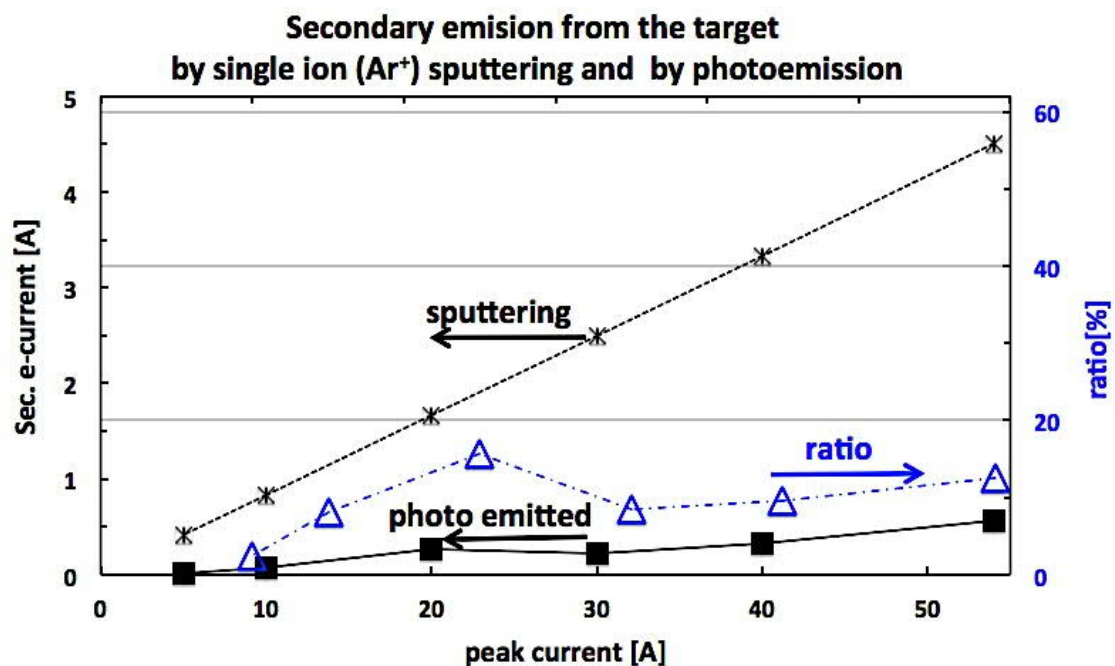


Figure 10. Sputtering produced and photo emitted electron current trends (in amperes) versus peak current. (Black star and left axis) is the sputtering current values produced by Ar^+ ions at the racetrack. (Black squares and left axis) the photo emitted current values

due to VUV irradiance for $\lambda < 135$ nm. (Blue triangles and right axis) the ratio of the photo emitted current divided by the sputtering current.

Albeit produced from a simple analysis, the inferred values for the total photocurrent shown in figure 10 are relevant to the topic of producing secondary electrons in HiPIMS targets. A conclusive comparison of sputtered versus photon emitted secondary electrons requires a more in depth analysis. This analysis could start determining which are the valid figures of merit, due to the continuous erosion of the target surface. Some of the issues that may play a relevant role are: a) what is the impact of the surface condition of the target surface as it recrystallizes while is heated during the plasma operation?, b) what is the effect of the target surface in the determination of the emission volume as an erosion profile is formed on the racetrack? and c) what is the impact of the angle of incidence on the photoemission coefficient?.

5. Conclusions

This work presents a novel method to determine *in situ* absolute values of UV/VUV photon rates from a HiPIMS plasma. The technique uses the measurement of the fluorescence produced by a NaSal layer to determine the photon rates from the plasma. The setup has a spatial resolution that is able to differentiate the boundary of the ionization region. Effective line of sight emissivities are estimated to test the soundness of the technique, assuming an ionization region in the shape of cylinder with the overall dimensions of the magnetic trap. The average irradiance values at the target in the VUV were: $7 \times 10^{18} \text{ s}^{-1} \cdot \text{cm}^{-2}$ produced mainly by Al^+ ions in the spectral region $135 < \lambda < 225$ nm and $2 \times 10^{18} \text{ s}^{-1} \cdot \text{cm}^{-2}$ produced by Ar^+ ions for $\lambda < 135$ nm. These irradiances at the cathode surface seem consistent with a linear scaling with electron density when compared to values measured in low-temperature and low-pressure plasmas. Since the VUV emission can extend to the entire target surface, the total photo emitted currents can reach 10-15% of the secondary electron current released by sputtering by single Ar^+ ions on the racetrack. Further studies addressing the role of the condition of the cathode surface in the photo production of secondary electrons are relevant to this discussion and are part of a future work.

Acknowledgments

We thank Marta Slapanska for help in doing the experimental measurements, and Julian Held for his comments in regard to the nature of the aluminum HiPIMS discharge. The authors gratefully acknowledge the support provided by the German Research Foundation within the framework of Transregional Collaborative Research Center TRR 87/1 (SFB- TR 87), “Pulsed high power plasmas for the synthesis of nano-structured functional layers”.

6. References

- [1] Nest D, Graves D, Engelmann S, Bruce R, Weirnboeck F, Oehrlein G, Andes C and Hudson E 2008 *Appl. Phys. Lett.* **92** 153113-3
- [2] Budde M, Corbella C, Große-Kreul S, de los Arcos T, Grundmeier G, Von Keudell A 2018 *Plasma Process Polym.* **15** e1700230 8pp
- [3] Shin H, Zhu W, Donnelly V M and Economou D J 2012 *J. Vac. Sci. Technol. A* **30**(2), 021306-10
- [4] Mitschker F, Dietrich J, Ozkaya B, de los Arcos T, Giner I, Awakowicz P and Grundmeier G 2015 *Plasma Proc. and Poly.* **212** 1002–9^[1]_{SEP}
- [5] Tian P and Kushner M 2017 *Plasma Sources Sci. Technol.* **26** 024005–23
- [6] Tian P and Kushner M 2015 *Plasma Sources Sci. Technol.* **24** 034017–28
- [7] Lundin D and Sarakinos K 2015 *J. Mat. Res.* **27** 12pp
- [8] Gudmundsson J T, Brenning N, Lundin D and Helmersson U 2012 *J. Vac. Sci. Technol. A.* **30** 35pp^[1]_{SEP}
- [9] Mahieu S, Ghekiere P, Depla D, Gryse R D, Lebedev O I and Tendeloo G V 2006 *J. Crystal Growth* **290** 8pp^[1]_{SEP}
- [10] Cormier P, Thomann A L, Dolique V, Balhamri A, Dussart N, R S, N L, T B, P S and Konstantinidis S 2013 *Thin Solid Films* **545** 6pp
- [11] Hecimovic A and von Keudell A 2018 *J. Phys D: Appl. Phys.* **51** 453001 15pp
- [12] Gallian S, Trieschmann J, Mussenbrock T, Brinkmann R P and Hitchon W N G 2015 *J. Appl. Phys.* **117** 8pp^[1]_{SEP}

- [13] Hecimovic A, de los Arcos T, von der Gathen V S, Boke M and Winter J 2012 Plasma Sources Sci. Technol. 21 035017 9pp
- [14] Iglesias E J, Mitschker F, Fiebrandt M, Bibinov N and Awakowicz P 2017 Meas. Science and Tech
- [15] Watanabe K and Inn E 1953 J. Opt. Soc. Am. 43 32–4^[SEP]
- [16] Seedorf R, Eichler H and Koch H 1985 Appl. Opt. 24 1135–42^[SEP]
- [17] Yushkov G Y and Anders A 2010 IEEE Trans. Plasma Sci. ^[SEP]**38** 3028–34
- [18] Bibinov N, Halfmann H, Awakowicz P and Wiesemann K 2007 Meas. Science and Tech. 18051327+11
- [19] K, Ralchenko Y, Reader J and Team N A Atomic spectra database (version 5.4) Available at <http://physics.nist.gov/asd>^[SEP]
- [20] Meier S M, Hecimovic A., Tsankov V T, Luggenhölscher D and Czarnetzki 2018 Plasma Sources Sci. Tech. 2018 27 035006 12pp
- [21] Kadlec S, 2007 Plasma Process. Polym **4** 5419-23 4pp
- [22] Vitelaru C, Lundin D, Stancu G D, Brenning N, Bretagne J and T Minea 2012 Plasma Sources Sci. Technol. **21** 025010 11pp
- [23] Kanitz A, Hecimovic A, Böke M and Winter J 2016 J. Phys. D: Appl. Phys. **49** 125203 11pp
- [24] Kozák T and Pajdarová A D 2011 J. Appl. Phys. **110**, 103303 11pp.
- [25] Hecimovic A and Ehasarian A 2011 IEEE Transactions on Plasma Science 39 4
- [26] Trieschmann J Contrib. Plasma Phys. 2018 **58** 394–403
- [27] Espinho S, Felizardo E, Henriques J, and Tatarova E 2017 J. Appl. Phys. **121**, 153303 11pp
- [28] Kunze H-J, *Introduction to Plasma Spectroscopy* 2009 Springer Verlag
- [29] Gudmundsson J T, Lundin D, Brenning N, Raadu M A, Chunqing Huo and T Minea T M 2016 Plasma Sources Sci. Technol. 25 065004 (18pp)
- [30] Hecimovic A, Held J, von der Gathen V S, Wolfgang Breilmann C M and von Keudell A 2017 J. Phys D: Appl. Phys. 50 505204 8pp^[SEP]
- [31] Merts A L, Mann J B, Robb W D and Magee N 1980 Los Alamos Sci. Lab (Rep.) No LA-8267-MS
- [32] Griffin D, Balance C, Loch S and Pinzola M 2007 J. Phys. B: At. Mol. Opt. Phys. **40**

4537 14pp

- [33] Woodworth J R, Riley M E, Amatucci V A, Hamilton T W and Aragon B P 2001 *J. Vac. Sci. Technol. A* **19** 45 11pp
- [34] Jinnai B, Fukuda S, Ohtake H and Samukawa S 2010 *J. Appl. Phys.* **107** 043302 6pp
- [35] Titus M J, Nest D and Graves D B 2009 *Appl. Phys. Lett.* **94** 171501 3pp
- [36] Boffard J B, Lin C, Culver C, Wang S, Wendt A E, Radovanov S and Persing H 2014 *J. Vac. Sci. Technol. A* **32** 021304 11pp
- [37] R. Piejak, V. Godyak, B. Alexandrovich, and N. Tishchenko 1998 *Plasma Sources Sci. Technol.* **7**, 590 9pp
- [38] D. Depla D, Heirwegh S, Mahieu S, Haemers J, and De Gryse R 2007 *J. App. Phys* **101**, 013301 9pp
- [39] D. Depla, G. Buyle, J. Haemers, R. De Gryse 2006 *Surf. Coat. Technol.*, **200** 4329 9pp
- [40] Clarke G C B, Kelly P J, Bradley J W 2005 *Surf. Coat. Technol.*, **200** 1341 4pp
- [41] Wendt A E and M A Lieberman *J. Vac. Sci. Technol. A* 1990 **8** 902, 5 pp
- [42] Samson J A R and Cairns R B 1965 *Rev. Sci. Inst.* **36** 19–21
- [43] Feuerbacher B and Fitton B^[1]_{SEP} 1972 *J. Appl Phys.* **43** 1563 9pp

